

Vitamin C-induced CO₂ capture enables high-rate ethylene production in CO₂ electroreduction

Received: 15 June 2023

Accepted: 20 December 2023

Published online: 02 January 2024

Check for updates

Jongyoun Kim^{1,4}, Taemin Lee^{1,4}, Hyun Dong Jung^{2,4}, Minkyung Kim¹, Jungsu Eo¹, Byeongjae Kang¹, Hyeonwoo Jung¹, Jaehyoung Park¹, Daewon Bae¹, Yujin Lee¹, Sojung Park³, Wooyul Kim³, Seoin Back²✉, Youngu Lee¹✉ & Dae-Hyun Nam¹✉

High-rate production of multicarbon chemicals via the electrochemical CO₂ reduction can be achieved by efficient CO₂ mass transport. A key challenge for C–C coupling in high-current-density CO₂ reduction is how to promote *CO formation and dimerization. Here, we report molecularly enhanced CO₂-to-*CO conversion and *CO dimerization for high-rate ethylene production. Nanoconfinement of ascorbic acid by graphene quantum dots enables immobilization and redox reversibility of ascorbic acid in heterogeneous electrocatalysts. Cu nanowire with ascorbic acid nanoconfined by graphene quantum dots (cAA-CuNW) demonstrates high-rate ethylene production with a Faradaic efficiency of 60.7% and a partial current density of 539 mA/cm², a 2.9-fold improvement over that of pristine CuNW. Furthermore, under low CO₂ ratio of 33%, cAA-CuNW still exhibits efficient ethylene production with a Faradaic efficiency of 41.8%. We find that cAA-CuNW increases *CO coverage and optimizes the *CO binding mode ensemble between atop and bridge for efficient C–C coupling. A mechanistic study reveals that ascorbic acid can facilitate *CO formation and dimerization by favorable electron and proton transfer with strong hydrogen bonding.

The electrochemical CO₂ reduction reaction (CO₂RR) to form value-added fuels and feedstocks is a promising route to achieve carbon neutrality and long-term energy storage¹. The development of CO₂RR electrocatalysts has led to advances in selectivity for multicarbon (C₂₊) chemicals such as ethylene (C₂H₄)^{2–4} and ethanol (C₂H₅OH)^{5,6} with high energy density and a high market price. However, it is a prerequisite to ensure profitability for the vitalization of CO₂RR-based chemical manufacturing. This requires an enhanced production rate for C₂₊ chemicals⁷. These chemicals are formed by C–C

coupling, which occurs via adsorbed carbon monoxide (*CO) dimerization on the surface of Cu active sites⁸. Although the product selectivity can be modulated by the design of active materials, including surface morphology, facet, defect, and alloy⁹, the production rate of CO₂RR products, especially for C₂₊ chemicals, is mainly affected by *CO formation on heterogeneous catalysts; the partial current density of C₂H₄ (*J*_{C₂H₄}) is proportional to the square of *CO coverage (θ_{CO}^2)¹⁰. In general, at the potential for high current density, the hydrogen evolution reaction (HER) becomes more dominant than

¹Department of Energy Science and Engineering, Daegu Gyeongbuk Institute of Science and Technology (DGIST), Daegu 42988, Republic of Korea.

²Department of Chemical and Biomolecular Engineering, Institute of Emergent Materials, Sogang University, Seoul 04107, Republic of Korea. ³Department of Energy Engineering, Institute for Environmental and Climate Technology, Korea Institute of Energy Technology (KENTECH), Naju 58330 Jeollanam-do, Republic of Korea. ⁴These authors contributed equally: Jongyoun Kim, Taemin Lee, Hyun Dong Jung. ✉ e-mail: sback@sogang.ac.kr; youngulee@dgist.ac.kr; dhnam@dgist.ac.kr

CO₂RR because of limited *CO coverage. Therefore, it has been a challenge to achieve CO₂-to-*CO conversion in high current density CO₂ electrolysis for high-rate C₂₊ chemical production.

CO₂-to-*CO conversion is significantly hampered by the limited *CO₂ formation, which is one of the main rate-determining steps (RDS) for the CO₂RR¹¹. To overcome this bottleneck, gas diffusion electrode (GDE)-based electrolyzers, such as flow cells and membrane-electrode-assembly (MEA), have emerged as an engineering approach to improve CO₂ transport to catalysts. GDE enables the supply of a large amount of CO₂ by providing gas flow directly to the electrocatalysts over the double- and triple-phase boundaries between gas CO₂, liquid electrolytes, and solid catalysts^{12,13}. In the GDE, micro-environment has been optimized in terms of CO₂ flow rate¹⁴, CO₂ partial pressure¹⁵, and catalyst architecture⁸. Also, molecular enhancement of CO₂RR by combining molecular additives with heterogeneous catalysts has recently received great attention. They contribute to increasing *CO coverage by enhancing CO₂ mass transport (increased local CO₂ concentration) or optimizing hydrophobicity^{2,3,16–24}. For instance, ionomers can provide CO₂ transport channels that increase the local CO₂ concentration near active sites and control the local pH and CO₂/H₂O ratio via selective ion conduction^{7,17,18}. Furthermore, polymers in molecularly augmented GDEs have been introduced to increase the local CO₂ concentration by optimizing porosity or hydrophobicity^{20,25}. However, the strategy to promote proton-coupled electron transfer-based *CO formation from CO₂ (g) has not yet been explored significantly for CO₂RR with high productivity in heterogeneous electrocatalysts.

Here, we report molecularly enhanced CO₂-to-*CO conversion and *CO dimerization for high-rate C₂H₄ production using ascorbic acid (AA). AA, also known as vitamin C, has been widely used as a reducing agent and antioxidant in nanomaterial synthesis and biochemical purposes^{26,27}. When we store fruits to preserve AA, maintaining a CO₂-deficient environment is essential because AA can react with CO₂ and be oxidized to dehydroascorbic acid (DHA) with proton and electron donation²⁸. Furthermore, AA has been utilized for CO₂ capture in homogeneous catalysis approaches^{29–31}. Inspired by this AA/DHA redox principle and CO₂ capture property, we exploited AA as a promoter to capture CO₂ near Cu, increase the *CO coverage and ensuing *CO dimerization on the surface of heterogeneous Cu catalysts.

To employ AA in heterogeneous catalysis with aqueous electrolytes, we pursued a strategy to immobilize water-soluble AA on electrocatalysts and achieve redox reversibility. We designed AA-augmented Cu nanowires (CuNWs) by applying graphene quantum dots (GQDs), which contain –OH and –COOH groups, as a mediator to anchor AA on the Cu surface with an ionomer. This nanoconfined AA on CuNW enhanced the CO₂-to-*CO conversion during the CO₂RR and resulted in high C₂H₄ productivity of heterogeneous Cu electrocatalysts. Unlike pristine CuNW (p-CuNW), which mainly produced C₂H₄ at low potential, CuNW with AA nanoconfined by GQDs (cAA-CuNW) boosted CO production over a similar potential range. As the potential increased for the high-current-density CO₂RR, enriched CO formation in cAA-CuNW was dramatically converted to C₂H₄, while the main electrolysis product of p-CuNW was hydrogen (H₂) because of limited CO₂ mass transport. We found that this enables efficient CO₂RR even in low CO₂ concentrations, which can be extended to the CO₂RR of flue gas. In situ Raman spectroscopy and operando X-ray absorption spectroscopy (XAS) studies enabled us to verify the effect of nanoconfined AA for inducing a high degree of *CO coverage and binding control between atop-bound CO (CO_{atop}) and bridge-bound CO (CO_{bridge}) on the reconstructed CuNW during the CO₂RR. Grand canonical density functional theory (GC-DFT) revealed that the redox of AA/DHA enabled efficient electron/proton transfer to CO₂ and multiple hydrogen bonding sites of AA, thereby improving CO₂-to-*CO conversion and *CO dimerization on Cu.

Results

Fabrication of vitamin C-augmented catalysts

AA-augmented CuNW was leveraged for high-rate CO₂-to-C₂H₄ conversion by nanoconfined AA on GQDs; favorable CO₂-to-*CO conversion and *CO dimerization on the Cu surface (Fig. 1a). For CO₂ capture, we harnessed the redox of AA/DHA; AA was oxidized and converted to DHA with electron and proton donation (Fig. 1b). A major bottleneck for the application of AA in heterogeneous catalysts is that AA is easily dissolved into the electrolyte due to its high solubility in aqueous solutions. Once it dissolves, it is difficult to reduce back to AA due to irreversible dehydration³². This stoichiometric consumption of AA degrades the sustainability of CO₂RR systems. Additionally, reversible redox of AA/DHA is required for efficient CO₂ capture. We improved the electroactive sustainability of AA by nanoconfined AA on GQDs. The confined AA ensures a redox-reversible environment through the improvement of the reduction reaction by DHA accumulation and stabilization in an aqueous electrolyte³².

Nanoconfinement of AA was achieved by the reaction between AA and GQDs at 95 °C to reduce and functionalize the GQDs³³. Note that excess reductant containing diverse oxygenated functional groups can remain on the reduced graphene surface and act as a multidentate hydrogen bonding donor^{34,35}. The reduced GQDs can form 2-dimensional supramolecular systems that could effectively confine AA via physisorption including π interaction or hydrogen bonding. (Supplementary Fig. 1). Then, AA-nanoconfined GQDs were combined with CuNW through mild sonication, and cAA-CuNW uniformly maintained the high-aspect-ratio structure of CuNW (Supplementary Fig. 2).

We fabricated p-CuNW, CuNW with GQD (G-CuNW), CuNW with AA (AA-CuNW) and cAA-CuNW to understand the role of nanoconfined AA on GQDs in the CO₂RR by comparing their catalytic reactions (Fig. 1c). Surface functionalization of CuNW was conducted by the interaction between the oxygen-containing functional groups of each reagent and the native oxide surface of the CuNW³⁶. The surface structures of CuNWs were investigated by scanning electron spectroscopy (SEM). Compared to p-CuNWs, surface-modified CuNWs showed a rough surface because of the existence of AA and GQDs. However, they exhibited similar 1-dimensional (1D) structures even after surface modification (Supplementary Fig. 3).

The crystalline structures of CuNWs were investigated by transmission electron spectroscopy (TEM) (Fig. 1d–k, Supplementary Fig. 4). High-resolution (HR)-TEM of p-CuNWs revealed the presence of crystalline Cu (Fig. 1d, e). G-CuNW showed a rough surface morphology because of the polycrystalline GQD assembly (Fig. 1f). This indicates that GQDs uniformly cover the surface of CuNW. The lattice distance of the polycrystalline outer shell in G-CuNW was 0.24 nm, which corresponds to the (100) plane of graphene (Fig. 1g)^{36,37}. AA-CuNW, composed of an amorphous shell with a thickness of ~3 nm, showed a more uniform surface than G-CuNW (Fig. 1h, i). The Cu surface of AA-CuNW was partially oxidized during surface functionalization because of the reaction with oxygen in an organic solvent (Supplementary Fig. 5). In the cAA-CuNW, both polycrystalline and amorphous regions coexisted, indicating that GQDs adequately confined AA on the surface of CuNWs (Fig. 1j, k). In the HR-TEM of CuNWs, lattice distance analysis and fast Fourier transform (FFT) confirmed the presence of pure Cu after surface functionalization (Supplementary Fig. 6).

Chemical states of vitamin C-augmented catalysts

We investigated the chemical states of CuNWs after nanoconfinement to verify the presence of AA and GQD. In the TEM energy-dispersive spectroscopy (EDS) mapping, all CuNWs showed a uniform distribution of C and O along the Cu, implying that the surface of the CuNWs was coated by each reagent (Supplementary Fig. 7). In the EDS spectrum for Cu, C, and O, the atomic fraction of C in G-CuNW was 12.6%, while O was barely detected (Fig. 2a and Supplementary Fig. 8).

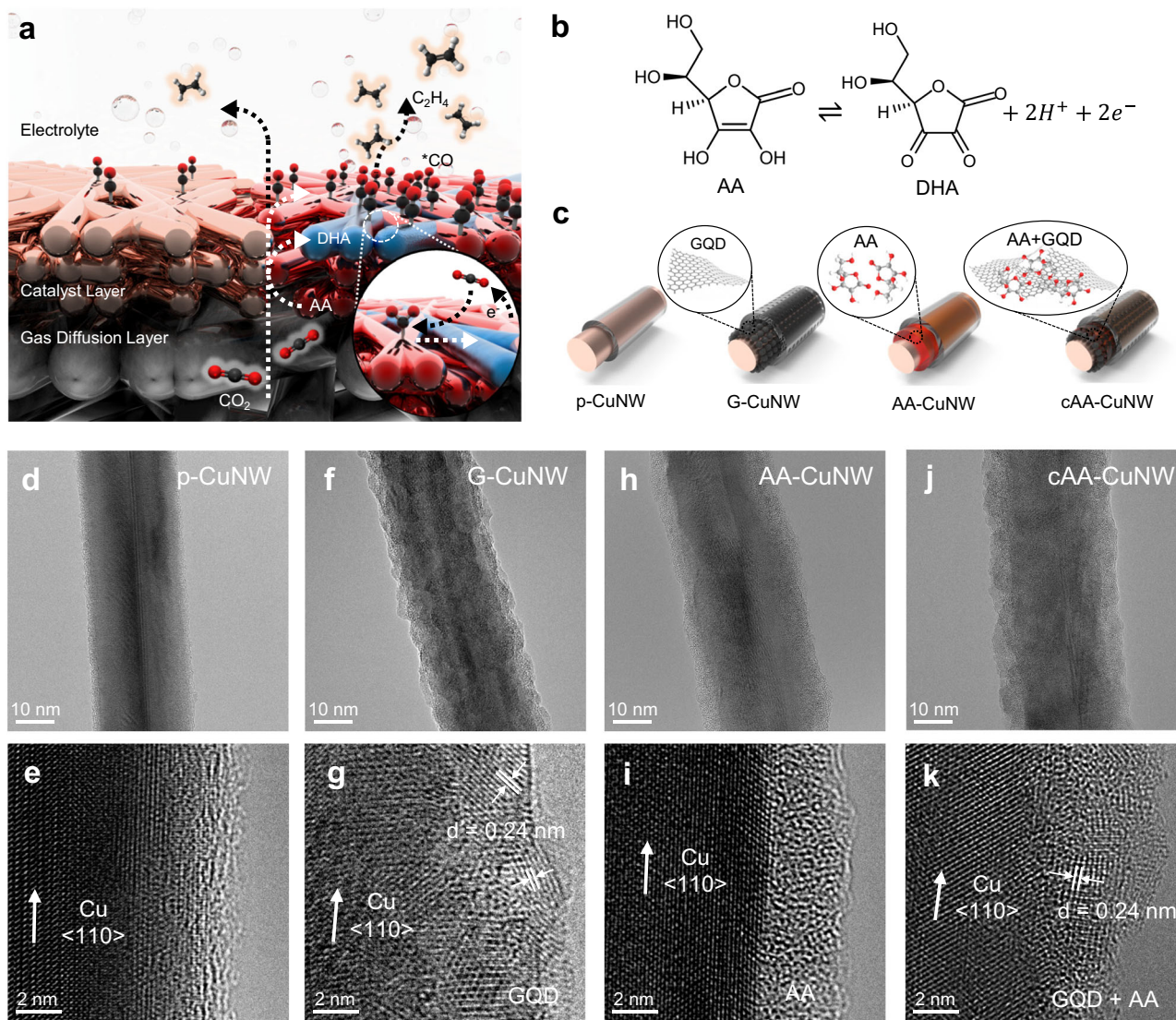


Fig. 1 | CO_2 capture strategy and surface structures of AA-augmented CuNWs. **a** Schematic of enhanced CO_2 -to- $^*\text{CO}$ conversion and $^*\text{CO}$ dimerization in cAA-CuNW for high-rate C_2H_4 production. **b** Redox of AA and DHA for CO_2 capture. **c** Schematic illustration of surface modification of CuNWs with GQD, AA, and

nanoconfined AA on GQDs. An ionomer is coated on the outer surface of CuNWs during the fabrication of the GDE. TEM (top) and HR-TEM (bottom) images of (**d**, **e**) p-CuNW, (**f**, **g**) G-CuNW, (**h**, **i**) AA-CuNW, and (**j**, **k**) cAA-CuNW.

However, the fraction of O (15.8%) was higher than that of C (7.0%) in AA-CuNW. In cAA-CuNW, the fraction of O was lower than that of C (20.1%) but still showed a significant ratio of 12.8%, suggesting the coexistence of GQDs and AA.

The presence of AA in cAA-CuNW was verified by X-ray photoelectron spectroscopy (XPS). The C 1s spectra of the G-CuNW showed a strong peak at -284.5 eV , which corresponds to the sp^2 C group of the GQDs (Fig. 2b). In addition, peaks for C–O and O–C=O bonds were observed at -285.8 and -287.7 eV , respectively, originating from the oxygenated C functional group at the edge of the GQDs^{30,37,38}. In the C 1s spectra of cAA-CuNW, the intensity of the peaks for C–O and O–C=O bonds increased, indicating that cAA-CuNW contains more oxygenated C groups than G-CuNW (Fig. 2c). Since these peaks were not observed in the C 1s spectra of GQDs separated from cAA-CuNW, the peaks for C–O and O–C=O bonds were attributed to the hydroxyl and carbonyl groups in AA (Supplementary Fig. 9).

In the Fourier transform infrared spectroscopy (FT-IR) analysis, we observed major peaks at approximately $1,666$, $1,365$, and $1,066 \text{ cm}^{-1}$, which corresponded to the C=C stretching vibration, C=C–O asymmetric stretching vibration of the enol-hydroxyl group, and C–O

vibration in the functional groups of AA in AA-CuNW and cAA-CuNW (Fig. 2d)³⁹. With TEM EDS, XPS, and FT-IR, comparison of thermogravimetric analysis (TGA) between G-CuNW and cAA-CuNW supported the presence of AA in cAA-CuNW (Supplementary Fig. 10). In the TGA of cAA-CuNW, an abrupt weight drop was observed at approximately $190 \text{ }^\circ\text{C}$, consistent with the decomposition temperature of AA⁴⁰. The X-ray diffraction (XRD) patterns of CuNWs exhibited a pure metallic Cu phase, indicating that the surface functionalization did not affect the chemical states of the active site in CuNWs (Fig. 2e). Consequently, it was inferred that AA is well confined on the surface of cAA-CuNW without any change in the chemical state of AA and Cu during surface modification.

We investigated the states of CuNWs after CO_2 RR through XRD, SEM, TEM, and TEM EDS. XRD patterns of all CuNWs showed Cu_2O (111) peaks due to the oxidation of metal surface by electrolyte contact after CO_2 RR (Supplementary Fig. 11). However, the 1D structures were maintained for all CuNWs as shown in SEM images (Supplementary Fig. 12), indicating that there was no significant structural transformation during CO_2 RR. The crystal structure and atomic distribution of CuNWs were analyzed using TEM and TEM EDS (Supplementary

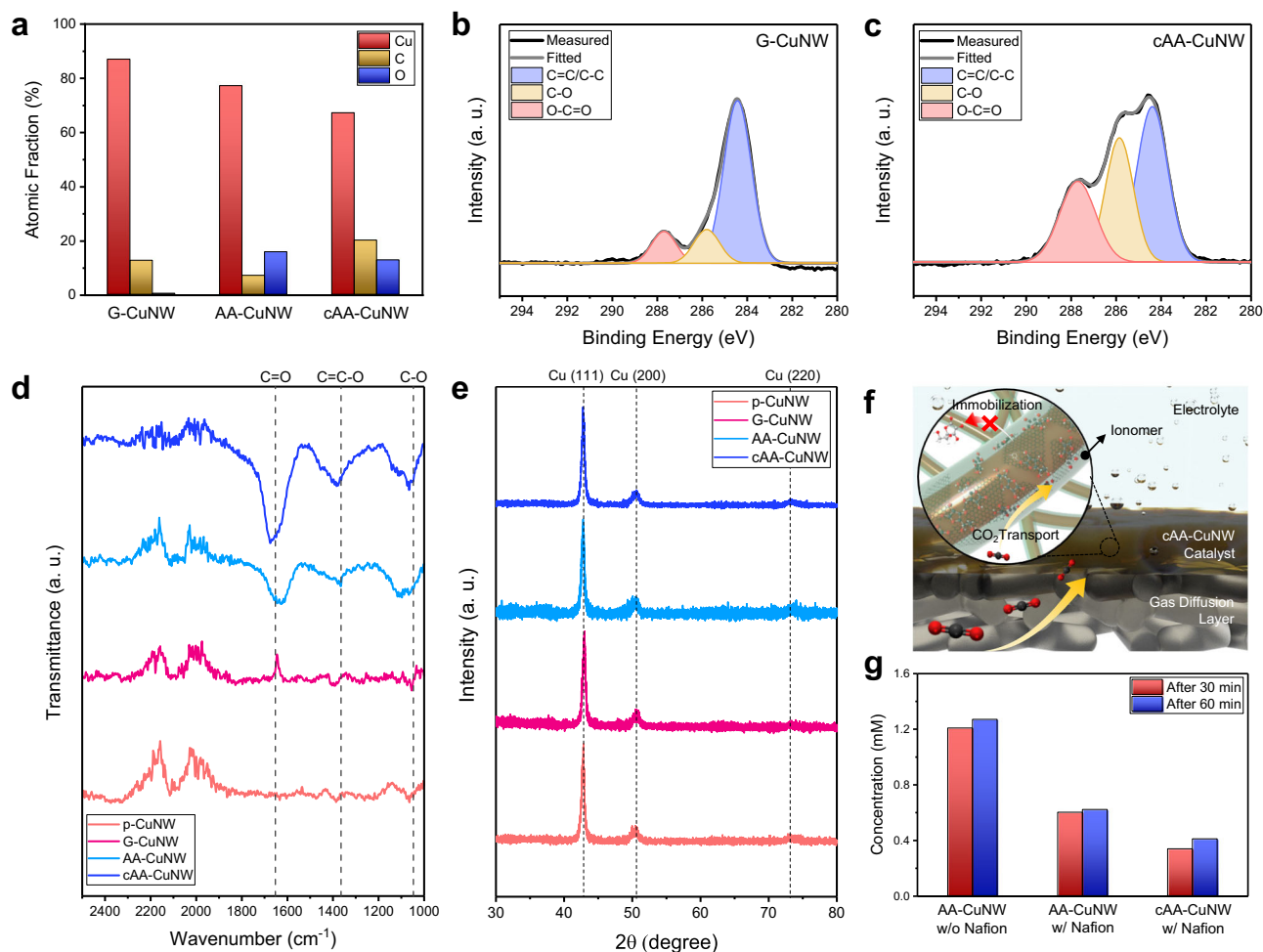


Fig. 2 | Chemical states of AA-augmented CuNWs. **a** Atomic fractions of Cu, C, and O for G-CuNW, AA-CuNW, and cAA-CuNW. **b** C 1s XPS spectra of (b) G-CuNW and (c) cAA-CuNW. **d** FT-IR spectra of p-CuNW, G-CuNW, AA-CuNW, and cAA-CuNW. **e** XRD patterns of p-CuNW, G-CuNW, AA-CuNW, and cAA-CuNW. **f** Conceptual schematic

of the surface components of Nafion ionomer-coated cAA-CuNWs for enhanced CO_2 -to- $^*\text{CO}$ conversion and $^*\text{CO}$ dimerization during the CO_2 RR. **g** Comparison of the amount of DHA extracted from AA-CuNW and cAA-CuNW with and without the Nafion ionomer coating. The extracted DHA concentration was analyzed by HPLC.

Fig. 13). CuNWs exhibited a rough Cu_2O surface after catalysis, which corresponds to the XRD analysis results. In addition, the lattice of GQDs and amorphous nanostructure of AA was still observed at the outer shell of G-CuNW, AA-CuNW, and cAA-CuNW, suggesting that each material was located on the CuNW surface during CO_2 RR. The elemental distribution in TEM EDS confirmed that the uniform distribution of Cu, C, and O atoms on the entire surface of the CuNW structure was maintained after CO_2 RR (Supplementary Fig. 14).

The redox reversibility of nanoconfined AA on GQDs was verified by cyclic voltammetry (CV) measured in a 1 M KOH electrolyte without gas supply (Supplementary Fig. 15). CV of nanoconfined AA on GQDs at the surface of a glassy carbon electrode (GCE) showed paired oxidation and reduction peaks after repetitive scans. Early in the cycle, a strong oxidation peak was observed due to the existence of excess AA, and these unconfined AAs were oxidized by repetitive scans. On the other hand, the CVs of intact GCE and GQD-coated GCE showed no significant redox peaks in the same potential window. When redox molecules are confined in nanocavities and their collision frequency with the electrode surface increases, the electrochemical reversibility is improved due to the enhancement of electron transport³². Therefore, we determined that the redox reversibility of AA was enhanced by the nanoconfinement effect through GQDs, ensuring sustainable electron and proton transfer during the CO_2 RR. Furthermore, we compared the CV of AA and nanoconfined AA on GQDs under N_2 and CO_2 gas (Supplementary Fig. 16). To minimize changes in CV curve due

to pH drop from bicarbonate formation, we proceeded CV with 0.1 M KHCO_3 electrolyte. Unlike AA, reversible AA/DHA redox is achieved in nanoconfined AA on GQDs under both N_2 and CO_2 gas. Therefore, we think that nanoconfined AA on GQDs can promote CO_2 -to- $^*\text{CO}$ conversion by enhancing electron and proton transfer from reversible AA/DHA redox during CO_2 RR (Supplementary Fig. 17).

To investigate the redox behavior of AA/DHA in the potential range of CO_2 RR, we analyzed linear sweep voltammetry (LSV) of nanoconfined AA on GQDs before and after CO_2 RR (Supplementary Fig. 18). We found that the most AAs were oxidized to DHA during LSV before CO_2 RR. However, the current density of peak for the oxidation of AA significantly increased after 24 h CO_2 RR at -1.8 V (vs RHE, non-iR corrected) (Supplementary Fig. 18b). This indicates that DHA was reduced to AA during CO_2 RR, regenerating AA to continuously promote CO_2 -to- $^*\text{CO}$ conversion in the potential range of CO_2 RR.

An increased local CO_2 concentration and immobilization of AA on the CuNW surface could be achieved by a perfluorosulfonic acid (PFSA) ionomer used for GDE fabrication with catalysts (Fig. 2f). When Nafion was coated on the catalyst, hydrophilic functional groups ($-\text{SO}_3^-$) preferentially interacted with the metal surface and formed hydrophobic domain ($-\text{CF}_2$) channels through which electrolytes and gases could be transported¹⁸. The effect of Nafion on promoting the immobilization of AA was investigated by quantitative analysis of DHA in aqueous solution extracted from each catalyst. To evaluate the protective role of Nafion via the impermeability of AA and GQD, AA-

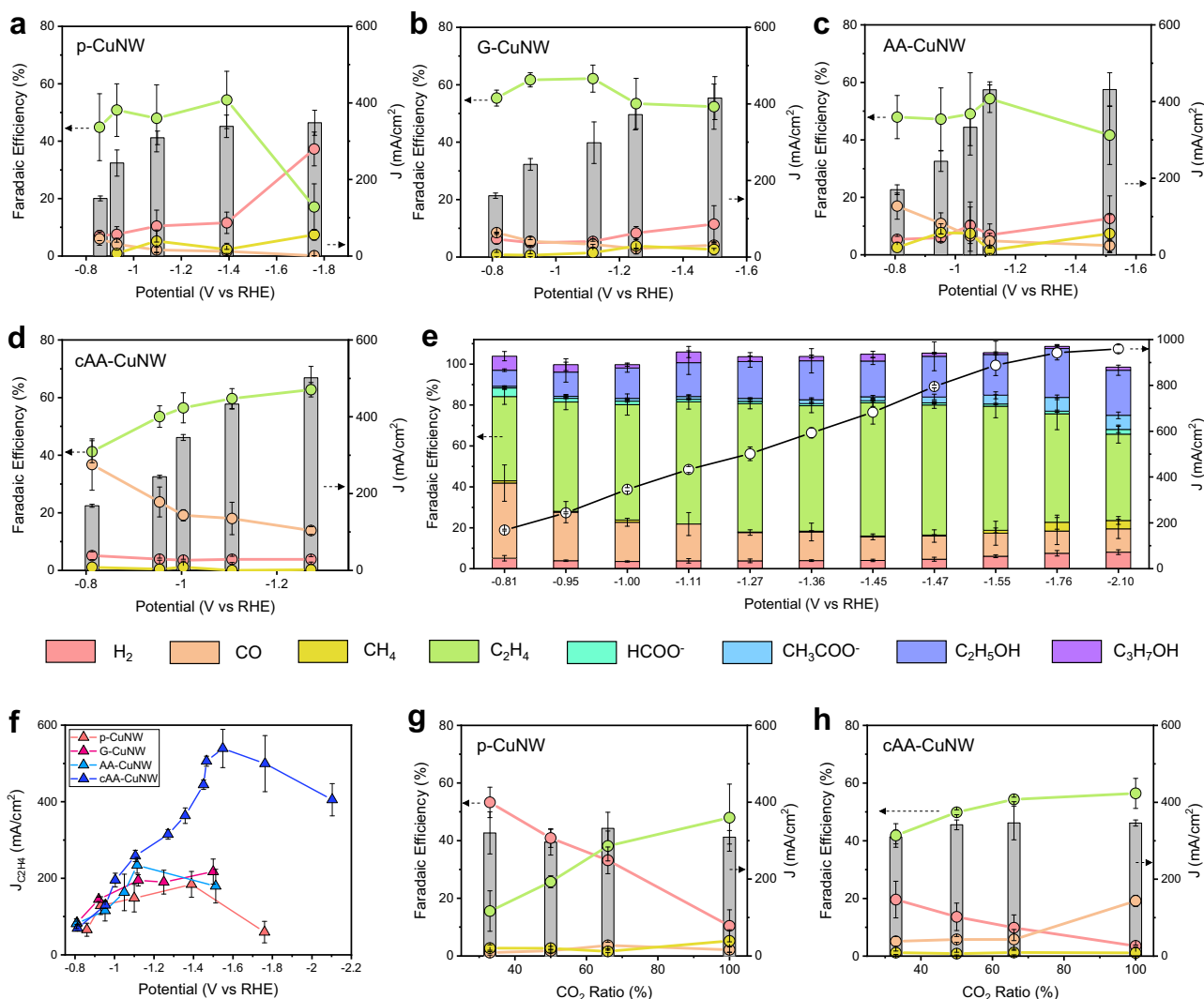


Fig. 3 | High-rate C_2H_4 production of cAA-CuNW by enhanced CO_2 -to- $*CO$ conversion and $*CO$ dimerization. Gaseous product FEs and total current densities for (a) p-CuNW, (b) G-CuNW, (c) AA-CuNW, and (d) cAA-CuNW in the CO_2RR with 1 M KOH electrolyte. e Total product FEs and total current densities for the cAA-CuNW with applied potentials up to -2.10 V (vs RHE). f Comparison of $J_{C_2H_4}$

versus potentials of p-CuNW, G-CuNW, AA-CuNW, and cAA-CuNW. Gaseous product FEs and total current densities of (g) p-CuNW and (h) cAA-CuNW in the CO_2RR according to CO_2 ratios in $CO_2 + Ar$ mixed gas. All the error bars represent standard deviation based on three independent samples.

CuNW and cAA-CuNW were prepared with and without Nafion coating. We quantified the extracted DHA by high-performance liquid chromatography (HPLC). DHA peaks were detected in the chromatographs of all catalysts at a retention time of -5.8 min because dissolved AA was easily oxidized to form DHA during the extraction process (Supplementary Figs. 19 and 20)³². The concentration of DHA extracted from AA-CuNW without Nafion was 1.27 mM after 1 hour of extraction (Fig. 2g). However, the concentration of DHA dramatically decreased for AA-CuNW (0.62 mM) and cAA-CuNW (0.41 mM) with Nafion. We expect that the immobilization of AA was promoted by the laminar arrangement of Nafion on CuNW, which helps to prevent AA from penetrating into the aqueous electrolyte⁴¹.

Electrochemical CO_2RR of vitamin C-augmented catalysts

The CO_2RR performances of the CuNWs were investigated in a flow cell electrolyzer with a 1 M KOH electrolyte (Fig. 3, Supplementary Figs. 22–25). In the p-CuNW, C_2H_4 was the main product at low potential ranges with a C_2H_4 Faradaic efficiency (FE) of 44.9% and CO FE of 6.1% at -0.86 V (Fig. 3a). However, when the potential exceeded -1.39 V (vs RHE) and reached -1.76 V (vs RHE), C_2H_4 FE decreased from

54.4 to 17.1%, and H_2 FE increased from 11.6 to 37.3% by limited CO_2 mass transport. G-CuNW showed more efficient C_2 product formation with a higher C_2H_4 FE of more than 50% than p-CuNW at a similar potential range (Fig. 3b). In addition, the maximum total current density of G-CuNW was 465 mA/cm² (Supplementary Fig. 25), higher than that of p-CuNW (348 mA/cm²). The enhanced total current density of G-CuNW is attributed to the existence of GQDs. Graphitic C shells can stabilize Cu active materials by alleviating reconstruction at a reductive potential^{4,42}. GQDs enhance the electrocatalytic activity, as the electron-donating functional group of GQDs promotes the activity of the CO_2RR by reducing the energy barrier of the RDS⁴³. Indeed, intact GQDs participated in the CO_2RR (Supplementary Fig. 26). However, we think that hindered gas diffusion⁴⁴ and hydrophilic nature of GQDs do not show a promotional effect on CO_2 mass transport (Supplementary Fig. 27). As a result, G-CuNW exhibited enhanced C_2H_4 selectivity in the low potential range with a maximum C_2H_4 FE of 62.1% at -1.12 V (vs RHE), but H_2 FE increased over 10%, and C_2 selectivity decreased as the potential increased to -1.50 V (vs RHE).

When the AA was hybridized to CuNW without GQD, we observed increased CO production in the low-potential range, which clearly

contrasts with the low CO production in p-CuNW and CuNW hybridized with DHA (DHA-CuNW) (Supplementary Fig. 28). AA-CuNW showed a CO FE of 17.0% at -0.81 V (vs RHE), while p-CuNW and G-CuNW showed CO FEs lower than 10% in a similar potential range (Fig. 3c). However, this increased CO formation did not contribute to *CO dimerization for C₂H₄ production in the high current density CO₂RR. Although CO FE decreased to 3.2% at -1.51 V (vs RHE), the H₂ FE increased to 12.6%, and the C₂H₄ FE decreased to 41.6% (Supplementary Fig. 24c). This may have originated from the absence of a nanoconfinement effect, which helped to prevent the dehydration of the AA and induce reversible AA/DHA redox, even when the Nafion ionomer prevented the AA from being dissociated by the electrolyte.

cAA-CuNW exhibited dramatically elevated CO production with an FE of 36.7% at -0.81 V (vs RHE). As the potential increased to -1.27 V (vs RHE), the CO FE decreased from 36.7 to 13.8%, and the C₂H₄ FE increased from 41.2 to 62.7% (Fig. 3d). The enhanced CO production implied that a large amount of *CO was formed on the catalyst surface. Since the formation rate of the C₂ product was proportional to θ_{CO}^2 , the evolved CO formation rate in cAA-CuNW could contribute to enhancing CO₂-to-*CO conversion for high-rate C₂H₄ formation. In particular, the ratio of C₂H₄ FE to methane (CH₄) FE (C₂H₄ FE/CH₄ FE) in cAA-CuNW is much higher than that of other CuNWs (Supplementary Fig. 29). This indicates that *CO dimerization is promoted in cAA-CuNW. In addition, cAA-CuNW showed a significantly low HER with an H₂ FE of 3.8% at -1.27 V (vs RHE). In cAA-CuNW, highly efficient C₂H₄ production was well maintained even when the potential reached -2.1 V (vs RHE) with a total current density of 960 mA/cm² (Fig. 3e).

When we compared partial current densities for H₂, CO, and C₂H₄, cAA-CuNW exhibited the highest C₂H₄ selectivity and productivity compared to other CuNWs; maximum J_{C₂H₄} of 539 mA/cm² with C₂H₄ FE of 60.7% at -1.55 V (vs RHE), which is 2.9-fold higher than the highest J_{C₂H₄} of p-CuNW with 184 mA/cm² at -1.39 V (vs RHE) (Fig. 3f and Supplementary Fig. 30). This is one of the highest J_{C₂H₄} values among previously reported Cu-based CO₂RR electrocatalysts (Supplementary Table 1). cAA-CuNW also showed the highest selectivity and productivity of CO and C₂H₄ in the electrochemically active surface area (ECSA)-normalized activity (Supplementary Figs. 31 and 32). The highest J_{C₂H₄} of cAA-CuNW is confirmed after considering the effect of surface roughness. This reveals that nanoconfined AA on GQDs promotes the intrinsic CO₂RR activity of cAA-CuNWs. We found that the overpotential at maximum J_{C₂H₄} can be lowered by increasing the concentration of electrolyte such as J_{C₂H₄} of 453 mA/cm², C₂H₄ FE of 56.3% at -0.57 V (vs RHE) in 2 M KOH electrolyte (Supplementary Fig. 33). However, when GQD and AA mixtures were deposited on the surface of CuNWs without any preceding reaction, there was no trend toward the enhancement of the production of CO and C₂H₄ (Supplementary Fig. 34). This revealed that the interaction between AA and GQD is key for the nanoconfinement effect, which can promote CO₂-to-*CO conversion and *CO dimerization by reversible AA/DHA redox and nanoconfined AA on GQDs.

Furthermore, we investigated CO₂RR of p-CuNW and cAA-CuNW in low CO₂ concentration by controlling CO₂ ratio in CO₂ + Ar mixed gas to further prove the effect of nanoconfined AA on CO₂-to-*CO conversion (Fig. 3g, h and Supplementary Fig. 35). As the CO₂ ratio decreased in the mixed gas, p-CuNW showed a dramatic increase of H₂ selectivity and decrease of C₂H₄ selectivity (H₂ FE of 53.3% and C₂H₄ FE of 15.6% at the CO₂ ratio of 33%). In contrast, cAA-CuNW exhibited H₂ FE of 19.6% and C₂H₄ FE of 41.8% even at the CO₂ ratio of 33%. Efficient C₂H₄ production of cAA-CuNW was maintained by promoted CO₂-to-*CO conversion even in low CO₂ concentration.

To confirm the stability of nanoconfined AA on GQDs in promoting CO₂RR, long-term CO₂RR was conducted in a flow cell electrolyzer with a 1 M KOH electrolyte (Supplementary Fig. 36). C₂H₄ selectivities of p-CuNW and cAA-CuNW were compared according to react ion times at a total current density of 300 mA/cm². C₂H₄ FE for

cAA-CuNW was maintained over 50% for 8 h, while that of p-CuNW abruptly decreased to 21.3% within 2 h. Also, similar FT-IR spectra of the GDE before and after the CO₂RR stability test confirmed that the nanoconfined AA on GQDs was stable in cAA-CuNW during CO₂RR (Supplementary Fig. 37). The CO₂RR stability of cAA-CuNW was further investigated in a zero-gap membrane electrode assembly (MEA) electrolyzer with 0.1 M KHCO₃ anolyte (Supplementary Fig. 38). cAA-CuNW exhibited outstanding stability of C₂H₄ production for 168 h at a total current density of 150 mA/cm². These results indicate that the nanoconfined AA is stably immobilized in cAA-CuNW and continuously promote CO₂-to-*CO conversion and *CO dimerization to enhance CO₂RR productivity.

Real-time analysis to track CO₂RR intermediates and Cu reconstruction

To study the origin of enhanced C₂H₄ productivity in cAA-CuNW, *in situ* Raman spectroscopy analysis was performed during the CO₂RR with a 1 M KOH electrolyte (Fig. 4, Supplementary Fig. 39). This enabled tracking of the interaction of *CO intermediates with the catalyst surface, as well as the *CO binding mode for C–C coupling. Specific Raman peaks were observed for *CO in the regions of 200–300, 300–400, 1950–2000, and 2050–2100 cm⁻¹, which were related to Cu–CO rotation, Cu–CO stretching, CO_{bridge}, and CO_{atop}, respectively^{45,46}. The other peaks observed at 525–534 and 615–630 cm⁻¹ of OCP were related to the interactions of the natural oxides with the Cu surface in CuNWs⁴⁷.

Securing the *CO intermediate on the active materials is important to maintain C₂ selectivity in the high current density CO₂RR. The surface *CO coverage of CuNWs was investigated by analyzing the Cu–CO binding peaks at 200–400 cm⁻¹. The origin of the Cu–CO binding peaks from CO₂ gas was confirmed through the comparison with *in situ* Raman spectroscopy under N₂ gas (Supplementary Fig. 40). cAA-CuNW, where nanoconfined AA on GQDs exists on the Cu surface, presented a significantly higher peak intensity for Cu–CO rotation and Cu–CO stretching than other CuNWs such as p-CuNW, G-CuNW, and AA-CuNW (Fig. 4a, c, e, g, and Supplementary Fig. 41). However, the peak intensities of p-CuNW were the lowest, which corresponds to the rapid increase of HER in the low-potential range⁴⁸. Considering that cAA-CuNW exhibited a lower *CO₂⁻ peak intensity at 1500–1600 cm⁻¹ compared to p-CuNW (Supplementary Fig. 42)⁴⁹, high *CO coverage of cAA-CuNW is attributed to the promoted CO₂-to-*CO conversion. To further investigate the effect of AA on *CO dimerization, we analyzed the Raman peaks for CO_{bridge} and CO_{atop} at -1950 – 2100 cm⁻¹, representing C≡O stretching of the adsorbed CO on the metal surface. The ratio between CO_{atop} and CO_{bridge} was strongly related to C₂ product selectivity^{2,50}. In general, the C–C coupling energy barrier decreased in the order of CO_{bridge} to CO_{bridge} > CO_{atop} to CO_{atop} > CO_{atop} to CO_{bridge}. Therefore, maintaining an optimal CO_{bridge}/CO_{atop} ratio is essential for efficient C₂₊ chemical production. In the C≡O stretching region, CO_{atop} and CO_{bridge} were simultaneously formed in AA-CuNW and cAA-CuNW at all CO₂RR potentials ranging from -0.4 to -0.8 V (vs RHE, non-iR corrected), whereas the CO_{bridge} peak almost disappeared as the reductive potential increased in p-CuNW (Fig. 4b, d, f, h, and Supplementary Fig. 41). We found that AA-CuNW and cAA-CuNW maintain adequate CO_{bridge}/CO_{atop} ratio even when the potential increases up to -0.8 V (vs RHE, non-iR corrected), while p-CuNW and G-CuNW exhibit excessive CO_{atop} or CO_{bridge} as potential increases (Fig. 4i). Note that strong Cu–CO binding peaks and optimal CO_{bridge}/CO_{atop} ratio in *in situ* Raman spectroscopy of cAA-CuNW were similarly observed under CO₂ + Ar mixed gas (Supplementary Fig. 43). Therefore, cAA-CuNW with C–C coupling between the CO_{bridge} and CO_{atop} ensemble facilitates *CO dimerization for C₂₊ chemical formation.

We investigated the reconstruction of Cu active materials in p-CuNW and cAA-CuNW by operando X-ray absorption spectroscopy (XAS) with a flow-cell-type reactor (Fig. 4j, k). We analyzed the

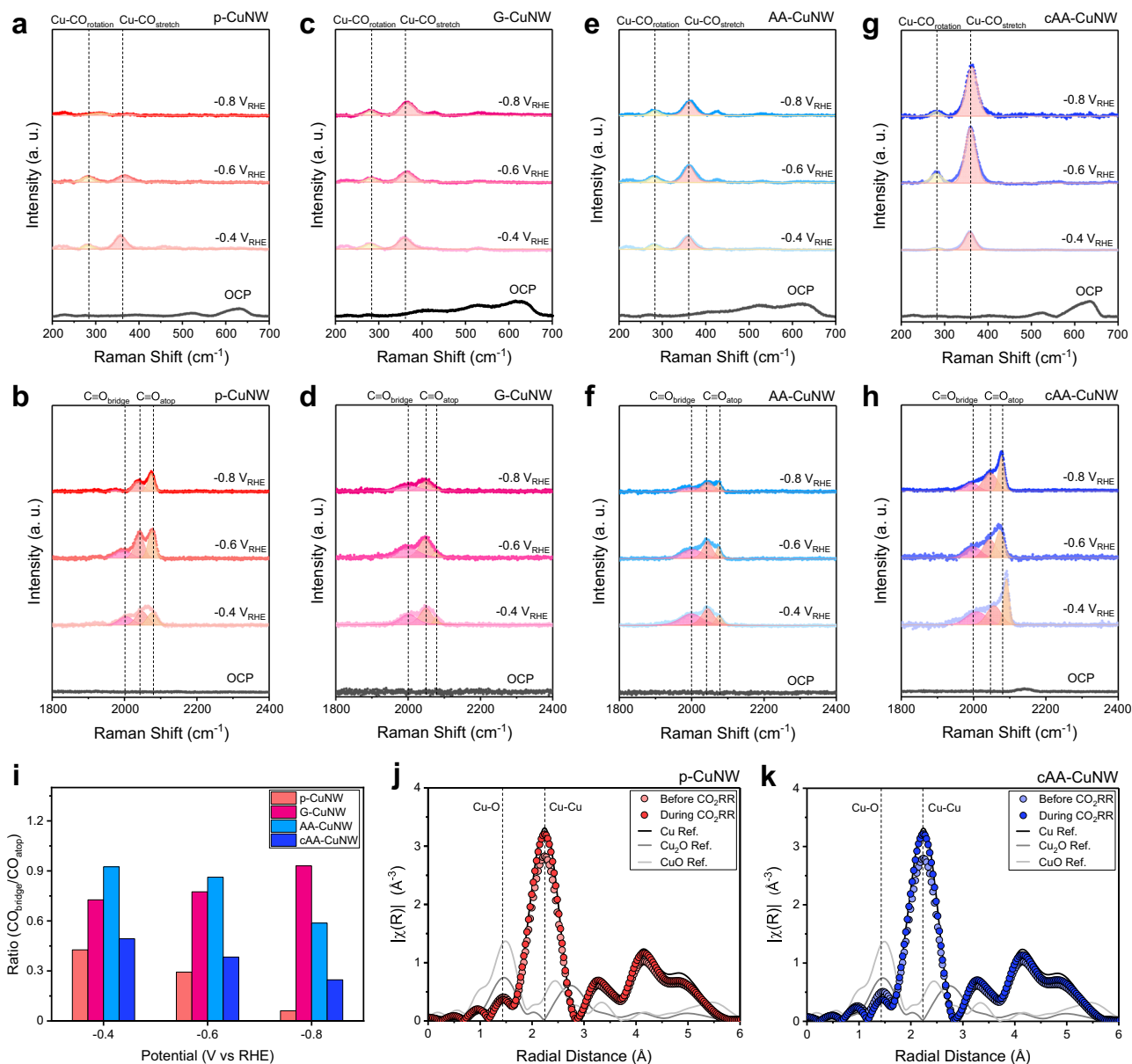


Fig. 4 | Real-time analysis of CuNWs with different degrees of surface hybridization during the CO₂RR. In situ Raman spectra of (a, b) p-CuNW, (c, d) G-CuNW, (e, f) AA-CuNW, and (g, h) cAA-CuNW obtained during CO₂RR according to the

applied potentials in the region of 200-700 cm⁻¹ (top) and 1,800-2,400 cm⁻¹ (bottom). **i** Comparison of integral area ratios of CO_{bridge} and CO_{atop} for CuNWs. Operando EXAFS spectra of (j) p-CuNW and (k) cAA-CuNW during the CO₂RR.

oxidation states and coordination number (CN) of Cu during the CO₂RR of CuNWs at a cathodic potential of -1.4 V (vs RHE, non-iR corrected) in a 1M KOH electrolyte. The Cu K-edge X-ray absorption near edge structure (XANES) spectra revealed that both p-CuNW and cAA-CuNW have the oxidation state of metallic Cu⁰, which was maintained during the CO₂RR (Supplementary Fig. 44). The CNs of p-CuNW and cAA-CuNW were investigated by extended X-ray absorption fine structure (EXAFS) spectroscopy (Fig. 4j, k and Supplementary Fig. 45). In the p-CuNW, the Cu-Cu bonding CN increased from 10.269 to 11.557 during the CO₂RR, indicating the reconstruction of Cu by reductive potential (Supplementary Table 2). We found that the Cu-Cu bonding CN of cAA-CuNW increased from 10.266 to 11.706, similar to that of p-CuNW. This similar Cu reconstruction between p-CuNW and cAA-CuNW revealed that nanoconfinement of AA on GQDs did not affect the Cu reconstruction behavior and that enhanced CO₂-to-*CO conversion and *CO dimerization originated from the augmentation of AA on CuNWs, not active materials.

Mechanistic study on the role of vitamin C in the CO₂RR

To understand the effect of AA on improved C₂₊ production, grand canonical density functional theory (GC-DFT) calculations were performed. We focused on the key steps of the electrochemical CO₂RR and compared the energetics and kinetics of Cu (100) with AA-decorated Cu (100), referred to as AA/Cu (100). The main steps include (1) CO₂ adsorption, (2) *COOH formation, (3) *CO formation, and (4) *CO dimerization. The competitive HER was additionally investigated. Note that easier *CO formation would increase *CO coverage on the surface, and more facile *CO dimerization would improve the selectivity of C₂₊ products.

We present the Gibbs free energy diagrams of each step at pH 14 and 0 V (vs RHE) (Fig. 5a). Both Cu (100) and AA/Cu (100) similarly preferred CO₂ chemisorption. One C-O bond was oriented parallel to the Cu surface (C-O_s) and the other C-O bond was bent toward the solvent (C-O_e), where O_s and O_e stand for oxygen atoms near the surface and the electrolyte, respectively (Supplementary Fig. 47). The

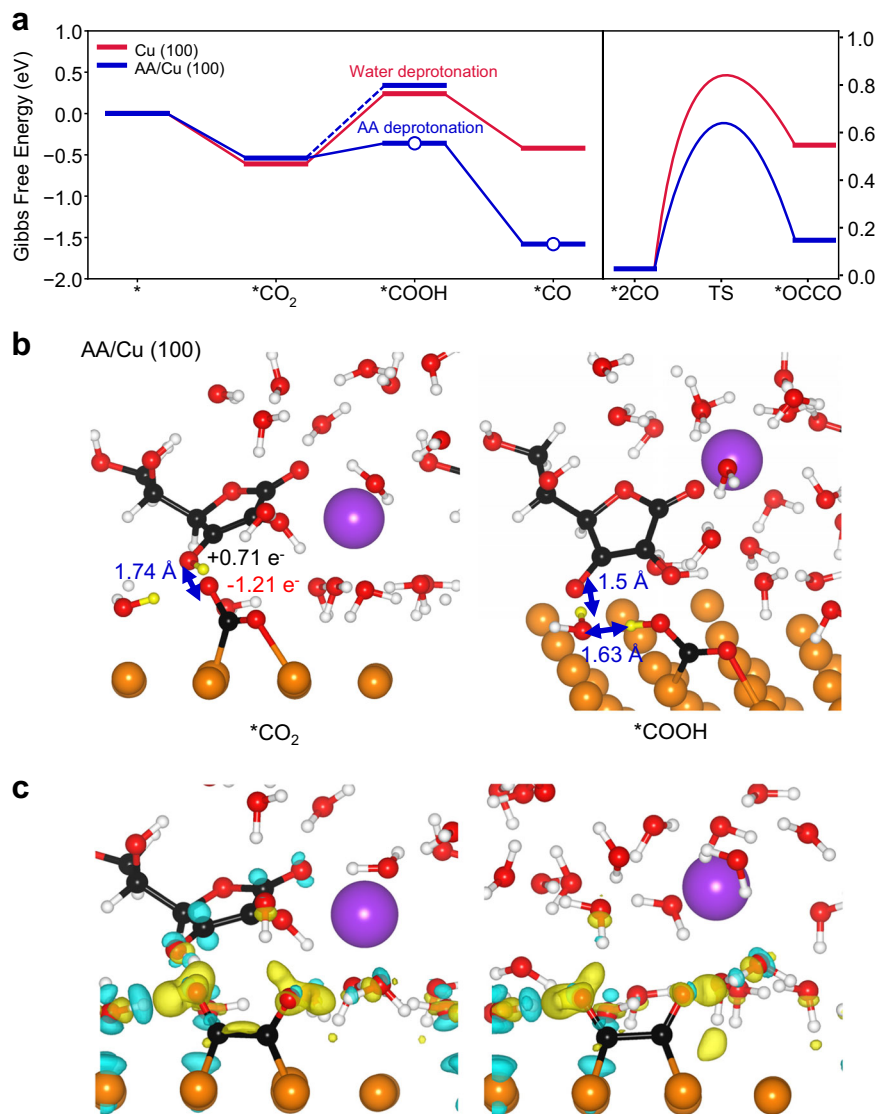


Fig. 5 | Computational modeling of the CO₂RR on Cu (100) and AA/Cu (100). **a** Gibbs free energy diagram of (left) CO₂-to-*CO conversion and (right) *CO dimerization at 0 V (vs RHE). White circles indicate the reaction pathway involving the deprotonation of AA. H₂O is the proton source otherwise. **b** The atomic structure of (left) the initial and (right) the final states of *CO₂ protonation from AA on AA/Cu (100) (*CO₂ + H₂O + AA + e⁻ → *COOH + H₂O + ASC⁻). **c** Charge density difference ($\Delta\rho$) of *OCCO adsorption on (left) AA/Cu (100) and (right) Cu (100).

Color code: black (C), white (H), yellow (H), red (O), purple (K), and orange (Cu). Yellow H atoms are considered for the protonation during the CO₂RR. The yellow and blue area represent an electron accumulation and depletion with an isosurface level of 0.005 e/Å³, respectively. The charge density difference is calculated as $\rho_{\text{total}} - \rho_{\text{ads+surf.}} - \rho_{\text{solv.}}$, where ρ_{total} , $\rho_{\text{ads+surf.}}$ and $\rho_{\text{solv.}}$ correspond to charge densities of the total system, the catalyst surface with adsorbates and solvent layers, respectively.

observed anisotropic configuration of the CO₂ adsorption is in consistent with literature⁵¹. The Bader charge analysis demonstrates that *CO₂ is highly negatively charged in both cases (-1.16 e⁻ on Cu (100) and -1.07 e⁻ on AA/Cu (100)), indicating a strong CO₂ adsorption due to the electron transfer (Supplementary Table 3)⁵².

The adsorbed *CO₂ is then protonated to form *COOH. On Cu (100), we considered a water molecule as the protonation source, and the reaction Gibbs energy ($\Delta G_{\text{CO}_2 \rightarrow \text{COOH}}$) was found to be endothermic (0.86 eV). On AA/Cu (100), we evaluated both the water molecule and AA as potential protonation sources (R2b for water and R2c for AA)⁵³. While the protonation from water exhibited a similar endothermic reaction Gibbs energy of 0.88 eV, protonation from AA proved to be thermodynamically more favorable, with a significantly lower reaction Gibbs energy ($\Delta G_{\text{CO}_2 \rightarrow \text{COOH}} = 0.18$ eV). This enhanced favorability can be attributed to lower pK_a value of AA (4.04)⁵⁴ compared to water (14), leading to a lower electrochemical deprotonation barrier⁵⁵.

To further elucidate the origin of the enhanced energetics, we inspected the adsorption configurations before and after the protonation. Before the protonation, on Cu (100), the hydrogen in the proton source was positively charged by +0.67 e⁻ and the hydrogen bonding distance ($d_{\text{O-H}}$) between O_e was 1.9 Å (Supplementary Fig. 48). In contrast, on AA/Cu (100), H_{OXI} exhibited a more positively charged state (+0.71 e⁻) and a shorter $d_{\text{O-H}}$ of 1.74 Å (Fig. 5b). After protonation, the hydrogen bonding network within the solid-electrolyte interface underwent significant reconstruction in the case of AA/Cu (100). The distance between O in water and H in *COOH was 1.63 Å, and the distance between H in water and O in ASC⁻ was 1.5 Å. However, on Cu (100), we did not observe a significant reconstruction following the protonation of *CO₂ from water. As a result, *COOH and ASC⁻ ion formed a more robust hydrogen bond network with water, thereby stabilizing the system. This observation suggests that the presence of AA promotes the favorable protonation of *CO₂ to *COOH. Further

protonation of *COOH to form *CO was energetically favorable in both cases, resulting in higher *CO coverages on AA/Cu.

We subsequently investigated the dimerization of *2CO, a key determinant of the selectivity of C₂₊ products such as C₂H₄⁵⁶. The dimerization of *2CO on Cu (100) was found to be endothermic, exhibiting the reaction energy of 0.52 eV and the activation energy of 0.81 eV. The introduction of AA on the surface decreased these energies to 0.13 eV and 0.62 eV, respectively, demonstrating that AA facilitates the dimerization. The charge density difference plot and the Bader charge analysis confirmed more significant electron transfer to *OCCO on AA/Cu (100) (−1.53 e[−] and +0.18 e[−] for adsorbate and Cu surface, respectively) compared to Cu (100) (−1.39 e[−] and +0.08 e[−]), making the interaction between *OCCO and the surface stronger through a more favorable electrostatic interaction (Fig. 5c)^{57,58}.

We also examined the competitive HER. The energetics of the first protonation step to form the adsorbed *H were found to be less favorable compared to *CO₂ adsorption, both with and without AA. Although the introduction of AA lowered the energy barrier of *H formation, the second protonation step remained unfavorable compared to *CO₂ adsorption (Supplementary Fig. 49). To sum up, GC-DFT calculations confirmed that the introduction of AA on Cu catalyst surface facilitated the CO₂RR, increasing *CO coverage on the surface and lowering the activation barrier of the rate-determining *CO dimerization, leading to higher production of C₂₊ products.

Discussion

We report vitamin C-induced CO₂ capture for effective CO₂-to-C₂H₄ conversion. AA was introduced to CuNWs for high rate C₂H₄ production by promoting electron and proton transfer and strong hydrogen bonding. By leveraging GQDs as a mediator to anchor water-soluble AA on CuNWs, we immobilized AA with an ionomer and enhanced the redox reversibility of AA, enabling sustainable CO₂ capture of AA for high-current density CO₂RR. This nanoconfined AA on Cu can steer the pathway toward C₂H₄ by securing CO₂-to-*CO conversion and *CO dimerization at high current density CO₂RR. cAA-CuNW exhibited higher CO selectivity than p-CuNW at a similar range of low electrolysis potential, indicating that nanoconfined AA effectively increased *CO coverage during the CO₂RR. cAA-CuNW demonstrated CO₂RR with a C₂H₄ FE of 60.7% and J_{C₂H₄} of 539 mA/cm² in 1 M KOH, 2.9-fold higher than the J_{C₂H₄} of p-CuNW. In the CO₂RR under CO₂ + Ar mixed gas (CO₂ ratio of 33%), cAA-CuNW exhibited C₂H₄ FE of 41.8% and H₂ FE of 19.6%, while p-CuNW exhibited C₂H₄ FE of 15.6% and H₂ FE of 53.3%. Efficient CO₂RR of cAA-CuNW at low CO₂ concentration confirms the promoted CO₂-to-*CO conversion, applicable to the CO₂RR of flue gas. In situ Raman spectroscopy and operando XAS revealed that enhanced *CO coverage and a judiciously controlled CO_{bridge}/CO_{atop} ratio for efficient C–C coupling was induced by the augmented AA on CuNWs. In GC-DFT, the Gibbs free energy diagram reveals that AA can facilitate *CO formation and dimerization by promoting electron/proton transfer and strong hydrogen bonding on the CuNW surface. This strategy can simultaneously contribute to optimizing *CO coverage for mass production of C₂₊ chemicals by combining with other molecular strategies for enhancing CO₂ mass transport in GDE. We believe that vitamin C-promoted CO₂ conversion, enabled by leveraging carbon mediators for bridging homogeneous and heterogeneous catalysis, can provide an avenue for compelling high-rate C₂₊ chemical manufacturing.

Methods

Nanoconfined AA on GQD preparation

GQDs (Sigma–Aldrich, 0.1 mg/mL) and L(+)-ascorbic acid (ACROS, 99%, 6 mM) were dissolved in 50 mL of D.I. water. Ammonia solution (Daejung Chemicals & Metals Co., 25%, 0.1 mL) was added to ensure the colloidal stability of the GQDs. The mixtures reacted at 95 °C for 1 h. Then, the solution was evaporated and redispersed in 5 mL of D.I. water.

Synthesis of the CuNWs and surface functionalization

CuNWs were prepared by hydrothermal methods⁵⁷. Anhydrous copper chloride (CuCl₂, Alfa Aesar, 13 mM), D-glucose (Sigma–Aldrich, 11 mM), and hexadecylamine (TCl, 56 mM) were dissolved in D.I. water (280 mL). The mixtures reacted in a hydrothermal reactor at 120 °C for 24 h and centrifuged with D.I. water. The product was then separated using hexane to collect CuNWs and dispersed in isopropyl alcohol (IPA). To prepare surface-functionalized CuNWs, 0.5 mL of GQDs, AA (5 mg/mL), or nanoconfined AA on GQDs was injected in methanol (20 mL). After adding CuNW solution (3 mg/mL, 2 mL), surface functionalization was conducted with mild sonication for 20 min. After that, the solution was washed with IPA by centrifuging at 2490 g for 15 min and stored in IPA.

Characterization of the CuNWs

The nanostructures of the catalysts were confirmed by an FEI Titan TEM (THEMIS Z, Thermo Fisher Scientific) operated at 300 kV. TEM sampling was performed by drop casting the catalysts on lacey formvar carbon-coated square Au grid. The crystal structures and chemical composition of the catalysts were analyzed by XRD (Miniflex 600 Mini, Horiba) and XPS (ESCALAB 250Xi, Thermo Fisher Scientific). XPS sampling was performed by drop casting of the catalyst on P type Boron doped Si wafer. For the characterizations of CuNWs after CO₂RR (XRD, SEM, TEM, TEM EDS), each electrode was operated in a flow cell electrolyzer at the applied potential of −3.2 V (vs Ag/AgCl) for 1 h (Supplementary Figs. 11–14). The redox reversibility of nanoconfined AA on GQDs was confirmed by an electrochemical analyzer (VSP, Bio-Logic). The electrode was prepared by coating 30 μL of nanoconfined AA on GQDs on a GCE with a radius of 3 mm. Then, 10 μL of Nafion was subsequently coated on the electrode to prevent dissolution into the electrolyte. The CV measurement was conducted using a three-electrode cell consisting of a Pt wire (counter electrode) and Ag/AgCl (reference electrode) with a scan rate of 50 mV/s. The chemical analysis of DHA after elution from the catalysts was performed by HPLC (Vanquish Core HPLC, Thermo Scientific). After sufficient chemical extraction by stirring the film in D.I. water, the extracted DHA was analyzed using an Aminex HPX-87H cation exchange column with a mobile phase of 0.5 mM sulfuric acid aqueous solution. The column temperature was maintained at 25 °C, and the flow rate was set at 0.6 mL/min. The chromatographic peaks were detected by a UV detector at a wavelength of 200 nm. The intermediates of the catalysts during the CO₂RR were analyzed by in situ Raman spectroscopy (XploRA™ PLUS Raman spectrometer, HORIBA). An altered flow cell with a water immersion objective lens (60×) and 785 nm laser were used. The CO₂ gas flow was fixed at 50 sccm by a mass flow controller (MFC). In situ Raman spectroscopy was measured up to the potentials of −0.8 V (vs RHE, non-iR corrected) due to laser focusing interference induced by gaseous products. The data were collected with an acquisition time of 10 s and acquired ten times in all measurements. Real-time analysis of the chemical states and bonding nature was performed by means of operando XANES and EXAFS. The XAS measurements were conducted at the 10 C X-ray beamline of Pohang Accelerator Laboratory (Pohang, Republic of Korea).

Electrode preparation and electrochemical CO₂RR measurement

Fifteen milligrams of CuNW were prepared as dispersed in IPA. Sixty microliters of Nafion ionomer (Sigma–Aldrich, 5 wt%) was mixed to increase both the immobilization of the catalysts and the CO₂ transport capacity. After vortex mixing, the solution was spray-coated on a porous polytetrafluoroethylene substrate (PTFE, Sterlitech) with an airbrush gun using N₂ gas to fabricate the GDE. To ensure uniform layer formation, spray coating was conducted on a 60 °C hot plate.

For the CO₂RR experiment, Ag/AgCl was used as the reference electrode, and Ni foam was used as the counter electrode. The anolyte

and catholyte were separated by the anion exchange membrane. The electrocatalytic CO₂RR performances of CuNWs were investigated at different cathodic potentials in a flow cell electrolyzer with a 1 M KOH electrolyte. The potential of Ag/AgCl was converted to RHE and the RHE conversion equation is as follows:

$$E_{\text{RHE}} = E_{\text{Ag/AgCl}} + 0.197(E^0) + 0.059 \cdot \text{pH} \quad (1)$$

We performed the calculation of 80% iR compensation losses between the Ag/AgCl and working electrode through electrochemical impedance spectroscopy (EIS) analysis.

The gas products of CO₂RR were analyzed by gas chromatography (GC, Micro GC Fusion, INFICON Inc.) equipped with two thermal conductivity detectors (TCDs) employing different carrier gases (argon and helium). The liquid products were analyzed by nuclear magnetic resonance spectrometry (NMR, Bruker). The mixture of catholyte, D₂O and dimethyl sulfoxide as an internal standard was collected in NMR tubes. The Faradaic efficiency of each product was calculated by the following equation:

$$\text{FE}(\%) = \frac{z \cdot n \cdot F}{Q} \quad (2)$$

where z and n are the number of electrons exchanged and moles of products, respectively; F is the Faradaic constant; and Q is the input charge. Gas product GC data per each sample were collected as the average value measured at 5, 30, and 55 min intervals. The error bars for CO₂RR data (gas and liquid products) represent standard deviation based on three independent samples. In the CO₂RR under CO₂ + Ar mixed gas, all measurements were conducted at the applied potential of -2.2 V (vs RHE, non-iR corrected) with 1 M KOH electrolyte. Gas flow rate was fixed to 60 sccm.

Grand canonical density functional theory (GC-DFT) calculations

The conventional calculation approach based on computational hydrogen electrode (CHE) method⁵⁹ simulates all systems at constant charge. Although this method is advantageous in understanding electrochemical processes with only a few DFT calculations^{60,61}, it could mislead the fundamental misunderstanding since the actual processes take place at a constant potential. This is because the systems described with the CHE method remain neutral during the electrochemical reactions, resulting in Fermi level fluctuations^{62,63}. The GC-DFT method adjusts the number of electrons in the systems, thus maintaining the Fermi level for all electrochemical reaction steps. This method essentially provides an accurate description of the electrode-electrolyte interface at a constant electrode potential^{64–66}.

To account for the combined effect of solvation and applied potentials, we treated the liquid-metal interface as a polarizable continuum using the linearized Poisson-Boltzmann equation, as implemented in VASPsol⁶⁷, where the Debye length was set to 3 Å, corresponding to a 1 M concentration of electrolytes with a relative permittivity of 78.4.

In this computational framework, we could tune the potential of the system by changing the number of electrons. The potential versus standard hydrogen electrode (U_{SHE}) was calculated as

$$U_{\text{SHE}} = (-\mu_e - \Phi_{\text{SHE}})/e \quad (3)$$

where μ_e and Φ_{SHE} correspond to the chemical potential of an electron and the work function of the standard hydrogen electrode (SHE), respectively. μ_e is defined as the Fermi level (ϵ_f) compared to the electrostatic potential of the bulk electrolyte (V_{bulk}) (Supplementary Fig. 50), and Φ_{SHE} was calculated to be 4.43 by RPBE⁶⁸. By changing the number of electrons, one can equate the μ_e of many states during the

electrochemical reactions, thus maintaining the potential. We set the convergence criteria for U to be 10⁻³ V.

The grand canonical electronic energy is calculated as

$$E_{\text{GC-DFT}} = E_{\text{DFT}} - \Delta n \mu_e - \Delta n V_{\text{bulk}} \quad (4)$$

where Δn is the number of electrons adjusted. Thus, Δn is positive (negative) when electrons are added (subtracted)^{58,69}.

Computational details

Spin polarized DFT calculations were performed using the Vienna Ab initio Simulation Package (version 5.4.4)⁷⁰. The generalized gradient approximation with the revised Perdew-Burke-Ernzerhof (GGA-RPBE) functional^{71,72} was used to describe the exchange-correlation interaction, and the D3 method of Grimme with a zero-damping function⁷³ was applied to include van der Waals interactions. The cutoff energy was set to 400 eV, and the convergence tolerances of energy and force were set to 10⁻⁴ eV and 0.05 eV/Å, respectively. (2 × 2 × 1) Monkhorst-Pack mesh of k -points⁷⁴ was sampled. We generated the initial guess of the transition state (TS) of *CO dimerization using the climbing image nudged elastic band (CI-NEB) method⁷⁵ with five intermediate images. Subsequently, we employed the dimer method⁷⁶ to converge the TS to the saddle point at the specific potential by adjusting the number of electrons.

To simulate the Cu catalyst surfaces, we fully relaxed a bulk structure of face-centered cubic (FCC) Cu. Subsequently, we constructed a three-layered (4 × 4) Cu (100) surface, with the bottom-most layer fixed to the bulk positions. To model the liquid-metal interfaces, we prepared 25 water molecules with one K⁺ ion^{11,77}. We then included a vacuum region of -12 Å in the z -direction to prevent any spurious interactions between repeating images. To obtain the liquid configuration, we conducted Ab-initio molecular dynamics (AIMD) simulations of a *CO₂ adsorbed Cu surface in the NVT ensemble using the Nose-Hoover thermostat for 5 ps, with a time step of 1 fs at 300 K. After confirming that the system had equilibrated, we optimized the last snapshot from the simulation and used it as the starting structural configuration. To model AA/Cu (100), we initially positioned AA approximately 3.5 Å above the surface according to the previous work on AA/Pd (100)⁷⁸, and then performed the AIMD simulations. Note that the optimized position of K⁺ is approximately 6 Å above the surface for both Cu (100) and AA/Cu (100). The AIMD simulations demonstrate that H_{OX1} is most closely positioned to the adsorbed *CO₂, suggesting that it is reasonable to assume the proton transfer of H_{OX1} in AA to adsorbates during the CO₂RR (Supplementary Fig. 51).

The grand canonical Gibbs free energy ($G_{\text{GC-DFT}}$) was calculated by adding Gibbs free energy correction values (G_{corr}) to $E_{\text{GC-DFT}}$. The correction values for adsorbates (gaseous molecules) were calculated using harmonic oscillator (ideal gas) approximations at 298.15 K in neutral systems as implemented in the Atomic Simulation Environment (ASE) (Supplementary Table 4)⁷⁹. To correct the gas-phase errors originating from the RPBE functional, we added +0.46 eV to the DFT energy of the CO₂ molecule⁸⁰.

Data availability

The data that support the findings of this study are available from the corresponding authors upon request. Source data for the figures in the main text are provided with this paper. Source data are provided with this paper.

References

- Ross, M. B. et al. Designing materials for electrochemical carbon dioxide recycling. *Nat. Catal.* **2**, 648–658 (2019).
- Li, F. et al. Molecular tuning of CO₂-to-ethylene conversion. *Nature* **577**, 509–513 (2020).

- Chen, X. et al. Electrochemical CO₂-to-ethylene conversion on polyamine-incorporated Cu electrodes. *Nat. Catal.* **4**, 20–27 (2021).
- Kim, J.-Y. et al. Quasi-graphitic carbon shell-induced Cu confinement promotes electrocatalytic CO₂ reduction toward C₂₊ products. *Nat. Commun.* **12**, 3765 (2021).
- Li, F. et al. Cooperative CO₂-to-ethanol conversion via enriched intermediates at molecule–metal catalyst interfaces. *Nat. Catal.* **3**, 75–82 (2020).
- Wang, X. et al. Efficient electrically powered CO₂-to-ethanol via suppression of deoxygenation. *Nat. Energy* **5**, 478–486 (2020).
- Zhao, Y. et al. Industrial-current-density CO₂-to-C₂₊ electroreduction by anti-swelling anion-exchange ionomer-modified oxide-derived Cu nanosheets. *J. Am. Chem. Soc.* **144**, 10446–10454 (2022).
- Xiao, C. & Zhang, J. Architectural design for enhanced C₂ product selectivity in electrochemical CO₂ reduction using Cu-based catalysts: a review. *ACS Nano* **15**, 7975–8000 (2021).
- Nitopi, S. et al. Progress and perspectives of electrochemical CO₂ reduction on copper in aqueous electrolyte. *Chem. Rev.* **119**, 7610–7672 (2019).
- Gao, D. et al. Activity and selectivity control in CO₂ electroreduction to multicarbon products over CuO_x catalysts via electrolyte design. *ACS Catal.* **8**, 10012–10020 (2018).
- Monteiro, M. C. O. et al. Absence of CO₂ electroreduction on copper, gold and silver electrodes without metal cations in solution. *Nat. Catal.* **4**, 654–662 (2021).
- Ren, S. et al. Molecular electrocatalysts can mediate fast, selective CO₂ reduction in a flow cell. *Science* **365**, 367–369 (2019).
- Weekes, D. M. et al. Electrolytic CO₂ reduction in a flow cell. *Acc. Chem. Res.* **51**, 910–918 (2018).
- Tan, Y. C., Lee, K. B., Song, H. & Oh, J. Modulating local CO₂ concentration as a general strategy for enhancing C–C coupling in CO₂ electroreduction. *Joule* **4**, 1104–1120 (2020).
- Bondue, C. J., Graf, M., Goyal, A. & Koper, M. T. M. Suppression of hydrogen evolution in acidic electrolytes by electrochemical CO₂ reduction. *J. Am. Chem. Soc.* **143**, 279–285 (2021).
- Nam, D.-H. et al. Molecular enhancement of heterogeneous CO₂ reduction. *Nat. Mater.* **19**, 266–276 (2020).
- Kim, C. et al. Tailored catalyst microenvironments for CO₂ electroreduction to multicarbon products on copper using bilayer ionomer coatings. *Nat. Energy* **6**, 1026–1034 (2021).
- García de Arquer, F. P. et al. CO₂ electrolysis to multicarbon products at activities greater than 1 A cm⁻². *Science* **367**, 661–666 (2020).
- Wagner, A., Sahm, C. D. & Reisner, E. Towards molecular understanding of local chemical environment effects in electro- and photocatalytic CO₂ reduction. *Nat. Catal.* **3**, 775–786 (2020).
- Wang, J. et al. Selective CO₂ electrochemical reduction enabled by a tricomponent copolymer modifier on a copper surface. *J. Am. Chem. Soc.* **143**, 2857–2865 (2021).
- Wei, X. et al. Highly selective reduction of CO₂ to C₂₊ hydrocarbons at copper/polyaniline interfaces. *ACS Catal.* **10**, 4103–4111 (2020).
- Liang, H.-Q. et al. Hydrophobic copper interfaces boost electroreduction of carbon dioxide to ethylene in water. *ACS Catal.* **11**, 958–966 (2021).
- Wakerley, D. et al. Bio-inspired hydrophobicity promotes CO₂ reduction on a Cu surface. *Nat. Mater.* **18**, 1222–1227 (2019).
- Lin, Y. et al. Tunable CO₂ electroreduction to ethanol and ethylene with controllable interfacial wettability. *Nat. Commun.* **14**, 3575 (2023).
- Xing, Z., Hu, X. & Feng, X. Tuning the microenvironment in gas-diffusion electrodes enables high-rate CO₂ electrolysis to formate. *ACS Energy Lett.* **6**, 1694–1702 (2021).
- Xiong, J., Wang, Y., Xue, Q. & Wu, X. Synthesis of highly stable dispersions of nanosized copper particles using L-ascorbic acid. *Green Chem.* **13**, 900–904 (2011).
- Song, J. et al. Synthesis of Au/graphene oxide composites for selective and sensitive electrochemical detection of ascorbic acid. *Sci. Rep.* **4**, 7515 (2014).
- Agar, I. T., Streif, J. & Bangerth, F. Effect of high CO₂ and controlled atmosphere (CA) on the ascorbic and dehydroascorbic acid content of some berry fruits. *Postharvest Biol. Technol.* **11**, 47–55 (1997).
- Arayachukiat, S. et al. Ascorbic acid as a bifunctional hydrogen bond donor for the synthesis of cyclic carbonates from CO₂ under ambient conditions. *ACS Sustain. Chem. Eng.* **5**, 6392–6397 (2017).
- Pastero, L. et al. CO₂ capture and sequestration in stable Ca-oxalate, via Ca-ascorbate promoted green reaction. *Sci. Total Environ.* **666**, 1232–1244 (2019).
- Pastero, L., Marengo, A., Boero, R. & Pavese, A. Non-conventional CO₂ sequestration via vitamin C promoted green reaction: yield evaluation. *J. CO₂ Util.* **44**, 101420 (2021).
- Choi, S. et al. Redox-transition from irreversible to reversible vitamin C by pore confinement in microporous carbon network. *ACS Appl. Mater. Interfaces* **14**, 36557–36569 (2022).
- De Silva, K. K. H., Huang, H.-H., Joshi, R. K. & Yoshimura, M. Chemical reduction of graphene oxide using green reductants. *Carbon* **119**, 190–199 (2017).
- Kwon, Y.-B. et al. Simultaneous reduction and functionalization of graphene oxide sheets with tannic acid for a strong composite material with multi-modally interactive interfaces. *Diam. Relat. Mater.* **119**, 108565 (2021).
- Kwon, Y.-B., Lee, S.-R., Seo, T. H. & Kim, Y.-K. Fabrication of a strong artificial nacre based on tannic acid-functionalized graphene oxide and poly(vinyl alcohol) through their multidentate hydrogen bonding. *Macromol. Res.* **30**, 279–284 (2022).
- Kim, J. et al. Ultrastable 2D material-wrapped copper nanowires for high-performance flexible and transparent energy devices. *Nano Energy* **106**, 108067 (2023).
- Ahn, Y., Jeong, Y., Lee, D. & Lee, Y. Copper nanowire–graphene core–shell nanostructure for highly stable transparent conducting electrodes. *ACS Nano* **9**, 3125–3133 (2015).
- Tang, L. et al. Bottom-up synthesis of large-scale graphene oxide nanosheets. *J. Mater. Chem.* **22**, 5676–5683 (2012).
- Pan, G.-H. et al. Photochemical reaction of vitamin C with silicon nanocrystals: polymerization, hydrolysis and photoluminescence. *J. Mater. Chem. C* **1**, 5856–5865 (2013).
- Jingyan, S., Yuwen, L., Zhiyong, W. & Cunxin, W. Investigation of thermal decomposition of ascorbic acid by TG-FTIR and thermal kinetics analysis. *J. Pharm. Biomed. Anal.* **77**, 116–119 (2013).
- Gerhardt, G. A. et al. Nafion-coated electrodes with high selectivity for CNS electrochemistry. *Brain Res.* **290**, 390–395 (1984).
- Li, Y. et al. Structure-sensitive CO₂ electroreduction to hydrocarbons on ultrathin 5-fold twinned copper nanowires. *Nano Lett.* **17**, 1312–1317 (2017).
- Zhang, T. et al. Regulation of functional groups on graphene quantum dots directs selective CO₂ to CH₄ conversion. *Nat. Commun.* **12**, 5265 (2021).
- Torrizi, L., Cutroneo, M., Torrizi, A. & Silipigni, L. Nitrogen diffusion in graphene oxide and reduced graphene oxide foils. *Vacuum* **194**, 110632 (2021).
- Chen, C. et al. Highly efficient electroreduction of CO₂ to C₂₊ alcohols on heterogeneous dual active sites. *Angew. Chem. Int. Ed.* **59**, 16459–16464 (2020).
- Chernyshova, I. V., Somasundaran, P. & Ponnurangam, S. On the origin of the elusive first intermediate of CO₂ electroreduction. *Proc. Natl Acad. Sci. USA* **115**, E9261–E9270 (2018).
- Deng, Y. & Yeo, B. S. Characterization of electrocatalytic water splitting and CO₂ reduction reactions using in situ/operando Raman spectroscopy. *ACS Catal.* **7**, 7873–7889 (2017).

48. Tadesse, L. F. et al. Toward rapid infectious disease diagnosis with advances in surface-enhanced Raman spectroscopy. *J. Chem. Phys.* **152**, 240902 (2020).
49. Zhao, Y. et al. Elucidating electrochemical CO₂ reduction reaction processes on Cu(*hkl*) single-crystal surfaces by in situ Raman spectroscopy. *Energy Environ. Sci.* **15**, 3968–3977 (2022).
50. Zhan, C. et al. Revealing the CO coverage-driven C-C coupling mechanism for electrochemical CO₂ reduction on Cu₂O nanocubes via operando Raman spectroscopy. *ACS Catal.* **11**, 7694–7701 (2021).
51. Cheng, T., Xiao, H. & Goddard, W. A. III Reaction mechanisms for the electrochemical reduction of CO₂ to CO and formate on the Cu(100) surface at 298 K from quantum mechanics free energy calculations with explicit water. *J. Am. Chem. Soc.* **138**, 13802–13805 (2016).
52. Ye, Y. et al. Dramatic differences in carbon dioxide adsorption and initial steps of reduction between silver and copper. *Nat. Commun.* **10**, 1875 (2019).
53. Shen, J. et al. Ascorbate oxidation by iron, copper and reactive oxygen species: review, model development, and derivation of key rate constants. *Sci. Rep.* **11**, 7417 (2021).
54. Williams, N. H. & Yandell, J. K. Outer-sphere electron-transfer reactions of ascorbate anions. *Aust. J. Chem.* **35**, 1133–1144 (1982).
55. Fan, L. et al. Proton sponge promotion of electrochemical CO₂ reduction to multi-carbon products. *Joule* **6**, 205–220 (2022).
56. Montoya, J. H., Shi, C., Chan, K. & Nørskov, J. K. Theoretical insights into a CO dimerization mechanism in CO₂ electroreduction. *J. Phys. Chem. Lett.* **6**, 2032–2037 (2015).
57. Calle-Vallejo, F. & Koper, M. T. M. Theoretical considerations on the electroreduction of CO to C₂ species on Cu (100) electrodes. *Angew. Chem. Int. Ed.* **52**, 7282–7285 (2013).
58. Lin, S.-C. et al. Operando time-resolved X-ray absorption spectroscopy reveals the chemical nature enabling highly selective CO₂ reduction. *Nat. Commun.* **11**, 3525 (2020).
59. Nørskov, J. K. et al. Origin of the overpotential for oxygen reduction at a fuel-cell cathode. *J. Phys. Chem. B* **108**, 17886–17892 (2004).
60. Peterson, A. A. et al. How copper catalyzes the electroreduction of carbon dioxide into hydrocarbon fuels. *Energy Environ. Sci.* **3**, 1311–1315 (2010).
61. Back, S., Kim, J.-H., Kim, Y.-T. & Jung, Y. Bifunctional interface of Au and Cu for improved CO₂ electroreduction. *ACS Appl. Mater. Interfaces* **8**, 23022–23027 (2016).
62. Kim, D., Shi, J. & Liu, Y. Substantial impact of charge on electrochemical reactions of two-dimensional materials. *J. Am. Chem. Soc.* **140**, 9127–9131 (2018).
63. Melander, M. M., Kuisma, M. J., Christensen, T. E. K. & Honkala, K. Grand-canonical approach to density functional theory of electrocatalytic systems: thermodynamics of solid-liquid interfaces at constant ion and electrode potentials. *J. Chem. Phys.* **150**, 041706 (2019).
64. Wang, Y., Liu, T. & Li, Y. Why heterogeneous single-atom catalysts preferentially produce CO in the electrochemical CO₂ reduction reaction. *Chem. Sci.* **13**, 6366–6372 (2022).
65. Alsunni, Y. A., Alherz, A. W. & Musgrave, C. B. Electrocatalytic reduction of CO₂ to CO over Ag(110) and Cu(211) modeled by grand-canonical density functional theory. *J. Phys. Chem. C* **125**, 23773–23783 (2021).
66. Choi, C. et al. Understanding potential-dependent competition between electrocatalytic dinitrogen and proton reduction reactions. *Nat. Commun.* **12**, 4353 (2021).
67. Mathew, K. et al. Implicit self-consistent electrolyte model in plane-wave density-functional theory. *J. Chem. Phys.* **151**, 234101 (2019).
68. Jinnouchi, R. & Anderson, A. B. Aqueous and surface redox potentials from self-consistently determined Gibbs energies. *J. Phys. Chem. C* **112**, 8747–8750 (2008).
69. Garza, A. J., Bell, A. T. & Head-Gordon, M. Mechanism of CO₂ reduction at copper surfaces: pathways to C₂ products. *ACS Catal.* **8**, 1490–1499 (2018).
70. Kresse, G. & Furthmüller, J. Efficiency of ab-initio total energy calculations for metals and semiconductors using a plane-wave basis set. *Comput. Mater. Sci.* **6**, 15–50 (1996).
71. Perdew, J. P., Burke, K. & Ernzerhof, M. Generalized gradient approximation made simple. *Phys. Rev. Lett.* **77**, 3865 (1996).
72. Hammer, B., Hansen, L. B. & Nørskov, J. K. Improved adsorption energetics within density-functional theory using revised Perdew-Burke-Ernzerhof functionals. *Phys. Rev. B* **59**, 7413 (1999).
73. Grimme, S., Ehrlich, S. & Goerigk, L. Effect of the damping function in dispersion corrected density functional theory. *J. Comput. Chem.* **32**, 1456–1465 (2011).
74. Monkhorst, H. J. & Pack, J. D. Special points for Brillouin-zone integrations. *Phys. Rev. B* **13**, 5188 (1976).
75. Henkelman, G., Uberuaga, B. P. & Jónsson, H. A climbing image nudged elastic band method for finding saddle points and minimum energy paths. *J. Chem. Phys.* **113**, 9901–9904 (2000).
76. Henkelman, G. & Jónsson, H. A dimer method for finding saddle points on high dimensional potential surfaces using only first derivatives. *J. Chem. Phys.* **111**, 7010–7022 (1999).
77. Shin, S.-J. et al. A unifying mechanism for cation effect modulating C1 and C2 productions from CO₂ electroreduction. *Nat. Commun.* **13**, 5482 (2022).
78. Yue, J., Du, Z. & Shao, M. The role of citric acid and ascorbic acid in morphology control of palladium nanocrystals: a molecular dynamics and density functional theory study. *Chem. Phys. Lett.* **659**, 159–163 (2016).
79. Larsen, A. H. et al. The atomic simulation environment—a Python library for working with atoms. *J. Phys. Condens. Matter* **29**, 273002 (2017).
80. Granda-Marulanda, L. P. et al. A semiempirical method to detect and correct DFT-based gas-phase errors and its application in electrocatalysis. *ACS Catal.* **10**, 6900–6907 (2020).

Acknowledgements

This work was supported by the National Research Foundation of Korea (NRF) grant funded by the Korean government (MSIT) (NRF-2021R1C1C1013784 and 2021M3D1A2047041, D.-H.N.). S.B. acknowledges the support from the National Research Foundation of Korea (NRF) funded by the Ministry of Education (NRF-2015M3D3A1A01064929, S.B.) and generous supercomputing time from KISTI. S.B. thanks Dr. Changhyeok Choi (University of Toronto) for helpful discussions on grand canonical DFT method. Y.L. acknowledges the support from Basic Science Research Program through the National Research Foundation (NRF) funded by the Ministry of Science and ICT (NRF-2018R1A5A1025594 and 2023R1A2C1003194, Y.L.). Y.L. also acknowledges the support from the BK21 FOUR program through the National Research Foundation (NRF) funded by the Ministry of Education of Korea. Experiments at PLS-II were supported in part by MSIT and POSTECH.

Author contributions

D.-H.N., Youngu L., and S.B. conceived and supervised the project. J.K. carried out sample synthesis and characterization. M.K. and B.K. assisted sample preparation. T.L. performed electrochemical CO₂RR, in situ Raman and operando XAS analysis. J.E. assisted electrochemical CO₂RR measurement. W.K., D.B., Yujin L., S.P. contributed to the real time analysis. H.J. and J.P. participated in data collection. S.B. and H.D.J. contributed to the DFT calculation and analysis. All authors discussed the results and contributed to writing the manuscript.

Competing interests

The authors declare no competing interests.

Additional information

Supplementary information The online version contains supplementary material available at <https://doi.org/10.1038/s41467-023-44586-0>.

Correspondence and requests for materials should be addressed to Seoin Back, Youngu Lee or Dae-Hyun Nam.

Peer review information *Nature Communications* thanks the anonymous, reviewers for their contribution to the peer review of this work. A peer review file is available.

Reprints and permissions information is available at <http://www.nature.com/reprints>

Publisher's note Springer Nature remains neutral with regard to jurisdictional claims in published maps and institutional affiliations.

Open Access This article is licensed under a Creative Commons Attribution 4.0 International License, which permits use, sharing, adaptation, distribution and reproduction in any medium or format, as long as you give appropriate credit to the original author(s) and the source, provide a link to the Creative Commons license, and indicate if changes were made. The images or other third party material in this article are included in the article's Creative Commons license, unless indicated otherwise in a credit line to the material. If material is not included in the article's Creative Commons license and your intended use is not permitted by statutory regulation or exceeds the permitted use, you will need to obtain permission directly from the copyright holder. To view a copy of this license, visit <http://creativecommons.org/licenses/by/4.0/>.

© The Author(s) 2024